SCIENCE ROBOTICS | RESEARCH ARTICLE

SOFT ROBOTS

Octopus-inspired sensorized soft arm for environmental interaction

Zhexin Xie[1,2]†, Feiyang Yuan[1]†, Jiaqi Liu[1]†, Lufeng Tian[1]†, Bohan Chen[1], Zhongqiang Fu[1], Sizhe Mao[1], Tongtong Jin[1], Yun Wang[1], Xia He[1], Gang Wang[1], Yanru Mo[1], Xilun Ding[1], Yihui Zhang[3], Cecilia Laschi[2], Li Wen[1]*

Octopuses can whip their soft arms with a characteristic "bend propagation" motion to capture prey with sensitive suckers. This relatively simple strategy provides models for robotic grasping, controllable with a small number of inputs, and a highly deformable arm with sensing capabilities. Here, we implemented an electronics-integrated soft octopus arm (E-SOAM) capable of reaching, sensing, grasping, and interacting in a large domain. On the basis of the biological bend propagation of octopuses, E-SOAM uses a bending-elongation propagation model to move, reach, and grasp in a simple but efficient way. E-SOAM's distal part plays the role of a gripper and can process bending, suction, and temperature sensory information under highly deformed working states by integrating a stretchable, liquid-metal–based electronic circuit that can withstand uniaxial stretching of 710% and biaxial stretching of 270% to autonomously perform tasks in a confined environment. By combining this sensorized distal part with a soft arm, the E-SOAM can perform a reaching-grasping-withdrawing motion across a range up to 1.5 times its original arm length, similar to the biological counterpart. Through a wearable finger glove that produces suction sensations, a human can use just one finger to remotely and interactively control the robot's in-plane and out-of-plane reaching and grasping both in air and underwater. E-SOAM's results not only contribute to our understanding of the function of the motion of an octopus arm but also provide design insights into creating stretchable electronics-integrated bioinspired autonomous systems that can interact with humans and their environments.

INTRODUCTION

Most soft-bodied animals owe their robotics-relevant dexterous movements to a "touch-perceive-execute" approach to interacting with the environment around them. Take the movement pattern of an octopus catching prey, with reaching and grasping motions, as an example. The octopus begins by bending an arm from the root. The bend propagates along the arm toward the prey following a simple but unique feed-forward wave of muscle activation from the brachial ganglia called "bend propagation" (*1*–*3*). Once a few suckers attach to the target, a highly sensitive sucker neural network triggers stopping and grasping signals (*4*, *5*). The arm's distal part wraps around the target and engages more suckers. A fetching movement is then elicited, which pulls the target toward the octopus' mouth. These reaching and grasping motions illustrate how octopuses can whip their long, sensorized arms to perform a gripping task. Mimicking this octopus behavior can create a valuable model for motor and control patterns of bioinspired soft robots when interacting with complex environments (*6*–*9*).

There are several major challenges to implementing such an integrated robotic system. First, achieving an effective bend propagation motion is essential. The octopus arm has an infinite number of degrees of freedom. Controlling such a redundant system is an exceedingly difficult task. Existing bioinspired robots have not yet achieved convincing experimental results in imitating an octopus's bend propagation (*10*–*13*). In particular, they are ineffective in controlling a soft robotic arm with multiple degrees of freedom (*2*, *14*–*16*). Second, the soft robotic system must integrate sensory, signal processing, and communication components to interact with the world around it. Although several technologies for flexible electronics (*17*–*20*) and electronics-free circuits (*21*, *22*) have been realized, integrating a stretchable electronic circuit with a highly deformable soft robot with multiple sensing capabilities (bending, suction, and temperature, for example) has not previously been reported.

In this work, we combine a sensing/processing network and the propagating motion of an octopus arm to create an electronics-integrated soft octopus arm (E-SOAM) capable of reaching, perceiving, and grasping (see the "Soft segments of E-SOAM" section for the detailed structure of E-SOAM). E-SOAM is pneumatically actuated and comprises a five-segment continuous soft arm and a distal part that plays the role of a terminal gripper, with an embedded electronic network. E-SOAM's terminal gripper has an on-body liquid metal network that mimics the functionality of an octopus nerve (*23*) and can process bending and sucker sensory information under highly deformable states. With a slender, tapered body, E-SOAM also uses the bend propagation strategy of an octopus to reach a target object. With the liquid metal–based stretchable electronic circuit, the robot can be bidirectionally controlled with a wearable finger glove that produces suction on a human finger (Fig. 1A). We show that a human can control the E-SOAM to reach and grasp in an underwater environment like octopuses do, by rotating the root of the arm to switch their reaching plane (*24*) (Fig. 1, B to E, and movie S1). When the human finger thrust leftward (Fig. 1B), the E-SOAM bend propagated to the left but failed to grasp the target, a floating toy shark (Fig. 1E), which "swam" away and escaped the predator

---

[1]School of Mechanical Engineering and Automation, Beihang University, Beijing 100191, China. [2]Department of Mechanical Engineering, National University of Singapore, Singapore 117575, Singapore. [3]Applied Mechanics Laboratory, Department of Engineering Mechanics, Laboratory of Flexible Electronics Technology, Tsinghua University, Beijing 100084, China.
*Corresponding author. Email: liwen@buaa.edu.cn

†These authors contributed equally to this work.

Fig. 1. E-SOAM for human interactive manipulation in complex environment. (**A**) A depiction of the E-SOAM's manipulation profile and design. The image shows an octopus performing its classical bending propagation. The arm and sucker nerves play an important role when the octopus captures prey. The E-SOAM robot displays a version of bend propagation to grasp a target. Liquid metal embedded in the terminal gripper mimics the octopus nerves and sensing ability. A human using a liquid metal–based soft wearable finger glove with bidirectional feedback loop. The haptic device generates haptic stimuli based on E-SOAM's suction sensation and sends them to a human user, who can in turn use this input to adjust their control of the E-SOAM. (**B** to **E**) Out-of-plane, human-operated E-SOAM sweeping and grasping underwater. (B) When the human operator thrusts a finger leftward, E-SOAM bend propagates to the left (E, t_1), and the floating toy shark "swims" away and escapes. (C) When the operator turns their elbow rightward and thrusts a finger down, E-SOAM rotates out of its original plane to the right (t_2). The operator then moves the finger to control the robot's bending (t_3), and suction haptic is generated on the human finger when suckers attach to the object on the surface of the water (t_4). (D) After the object is stably grasped (t_5), it is pulled back into the water (t_6).

(t_1). When the operator turned his elbow rightward (t_2) and thrust his finger down (t_3) (Fig. 1C), the E-SOAM rotated out of the plane (t_2) and bent the terminal gripper to grasp the object floating on the surface (t_3) until suction haptic generated on the human finger when the toy shark was attached (t_4). The toy shark was then stably gripped (t_5) and lastly pulled back into the water (t_6), all controlled by finger motion (t_5) (Fig. 1D). The parameters used to control the E-SOAM and sensory data are given in fig. S16 (B to D) and the "Reaching and sweeping trials" section.

In this study, we demonstrate a closed loop between the environment, the robot, and a human by evaluating E-SOAM's sensing and processing capabilities when interacting with its environment, investigating E-SOAM's bending propagating functionality both in air and underwater, and implementing bidirectional interaction between the human and robot via haptic feedback.

RESULTS

Terminal gripper with embedded electronics

E-SOAM's soft terminal gripper contains liquid metal electronics that can sense, process, and wirelessly transmit bending, suction, and temperature signals (Fig. 2A). We implemented a highly stretchable electronic circuit containing multiple sensing elements (including both bending and suction), electrodes, silicon integrated circuit (IC) chips, resistances, and diodes, for example. One major challenge was that the delamination failure occurred at the junction between the soft substrate and the silicon electronic components when stretched to a large extent (140% uniaxially) (fig. S3, B and C) (*25*). We addressed this by introducing a gradient material design to relieve the stress concentration in the vicinity of the ICs, which can be realized using a liquid metal planographic printing approach (fig. S1 and the "Fabricating a liquid metal–based stretchable electronic circuit" section).

We performed finite element analysis (FEA) simulations to calculate the maximum principal strain along the line where the circuit's middle plane crossed the top surface of the rigid chips and measured the effect of the shape of the intermediate material on the strain associated with the stretchable electronic circuit (fig. S2 and the "Intermediate material optimization" section). We found that the strain at the interfaces between the soft substrate and ICs was notably reduced by introducing gradient materials (Fig. 2B). An optimized stretchable circuit test unit could function when stretched up to 710%, a notable increase beyond the maximum length of 350% for an unoptimized unit (Fig. 2C). Furthermore, the optimized stretchable electronic circuit composed of both sensing parts and ICs could function under uniaxial stretching (up to 360%; movie S2) and biaxial stretching (inflated up to 270% beyond the original area; movie S3) and in an aquatic environment (fig. S3 and the "Stretching tests of the stretchable electronic circuit" section).

We integrated the stretchable electronics on top of the soft terminal gripper (*26*) surfaces and embedded the patterned liquid metal sensors into the suckers (fig. S4 and the "Fabricating of the sensorized terminal gripper" section). The underwater adhesion performance of the terminal gripper is provided in fig. S6. As a result, the gripper could sense and reconstruct the bending curve with a kinematics model based on real-time feedback from the elongation (EL) and expansion (EP) sensors (Fig. 2D; fig. S7, A to G; movie S4; and the "Kinematic reconstruction of the bending terminal gripper" section). Regarding a sucker's sensory system, we found that the contact surface squeezes the rim of a sucker and results in deformation (fig. S4E), leading to a change in the resistance of the embedded liquid metal channels (fig. S4F). We compared three designs for this system with different geometries (fig. S4G) and found that the design with more dentitions results in a notably higher resistance change during attachment and detachment (Fig. 2E). Additionally, each sucker can sense attachment and detachment, giving the terminal gripper more contact awareness (fig. S7, H to J). After we inserted a thermo-sensing chip inside the sucker, the sucker could sense the temperature of a nearby hot object (Fig. 2F). We also verified the reliability of the suction and temperature sensors while operating the gripper. We found that the suction and temperature sensory outputs are not affected by the circuit's stretching during the actuation of the gripper (fig. S8 and the "Evaluating the sensing ability of the suckers" section).

The terminal gripper can autonomously perform a task in an artificially confined environment. We first mounted the gripper on a commercial robotic arm to do so. The gripper detected a barrier in front of the arm and identified the entrance gap by bending (Fig. 2G). After the gripper entered the confined space, it determined the direction of an illuminated bulb and followed a temperature gradient to approach the bulb (Fig. 2I). Once suckers detected attachment (Fig. 2J), the gripper inflated and bent to turn off the bulb (Fig. 2H). The bending and suction sensory feedback of the entire autonomous operation process is shown in Fig. 2K (for a detailed working flow, see fig. S9, table S1, and movie S5).

Soft arm's bend propagation

E-SOAM also needed to perform a bend propagation motion along its arm to deliver the proprioceptive terminal gripper to a target at a distance. We studied the kinetics of a biological octopus to develop a simple and reprogrammable model for the soft arm. We made animal observations in which the octopus unfolded its arm with a bending point that moved from the root to the tip of the arm, creating in-plane bending wave propagation (*24*). The posture of the arm could be determined by four key variables: the total length of the arm $l(t)$, the distance between the bending point and the root of the arm $l_1(t)$, the bending curvature $\kappa(t)$, and the deflection angle $\theta_0(t)$, which is the angle of connection between the arm root and the bending point (fig. S11, A to C). For $l(t)$ and $l_1(t)$, we used a normalized original arm length l_0 and a normalized time t.

We noticed that the arm propagation deflection angle $\theta_0(t)$ varied notably between different bend propagation trails of the octopus. We here defined two modes of propagating motion divided by the angle variation $\Delta\theta_0 = 20°$ from 24 trials: a straightforward point-to-point reaching motion with a $\Delta\theta_0$ smaller than 20° (average of 12°) (Fig. 3, A and C, and movie S6) and a large sweeping motion with a $\Delta\theta_0$ larger than 20° (average of 53°) (Fig. 3, B and D, and movie S7). The reaching motion delivered the terminal gripper to a target's precise location following a short path; the sweeping motion delivered the terminal gripper while enlarging the path area of the arm. From all 24 observations, both reaching and sweeping motions were executed with the octopus arm length changing $\Delta l/l_0$ (average of 0.53) (fig. S11H) (*3*).

We introduced the classical "rose line" equation in polar coordinates to model these two modes (reaching and sweeping) of bend propagation

$$f(t) = \{\rho(\theta) = k_1 \sin(k_2(\theta - \theta_0(t))) \mid \theta_0(t) < \theta < \theta_m\} \quad (1)$$

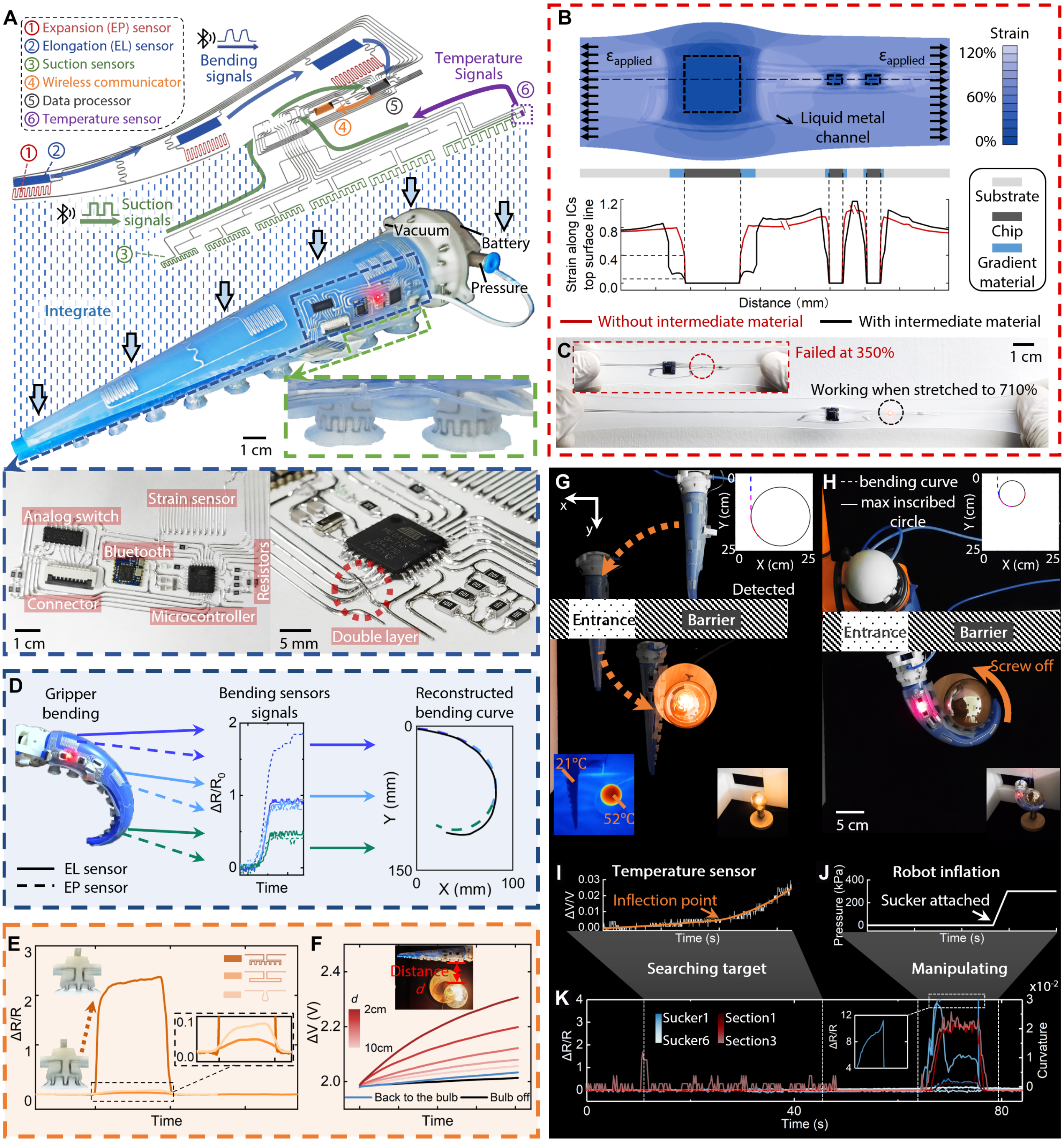

Fig. 2. The soft robotic terminal gripper embedded with a liquid metal electronics system. (**A**) Design of the integrated liquid metal electronics embedded in the terminal gripper, which can sense both bending (through elongation and expansion sensors) and suction, process those signals on board, and wirelessly transfer them. Details of the printed stretchable electronic circuit and embedded liquid metal are shown. (**B**) Realization of a highly stretchable electronic circuit system for soft robots. By integrating material ($E_2 = 660$ kPa) between the soft substrate ($E_1 = 69$ kPa) and rigid chips, the finite-element simulation shows that strain between the contact interface of the chip and soft substrate is largely reduced. (**C**) The optimized liquid metal circuit functioned under 710% strain; the inset panel shows that the circuit without intermediate material failed when stretched to 350% (LED light off). (**D**) The bending profile of the terminal gripper reconstructed from the feedback data of the bending sensors, a pair of EL and EP sensors. (**E**) Progression of sensory feedback from different types of liquid metal circuits during sucker attachment (and detachment). (**F**) The sucker can sense the temperature of an approaching hot object. (**G**) The robot autonomously explored an unknown environment and performed a mission over several steps. First, the robot identified and navigated through an entrance gap on the basis of feedback from bending sensors. (**H**) The robot then approached the illuminated bulb with the help of its temperature sensor. The XY plots in (G) and (H) show the reconstructed bending curve of the gripper. The circle represents the maximum inscribed circle of the bending curve. (**I**) The feedback of the temperature sensor over time. The inflection point indicates when the heating rate of the sucker increased as the gripper faced the bulb. (**J**) The robot curled and screwed off the bulb once the suckers attached to the bulb's surface. (**K**) The bending and suction sensory feedback plotted versus time throughout this process.

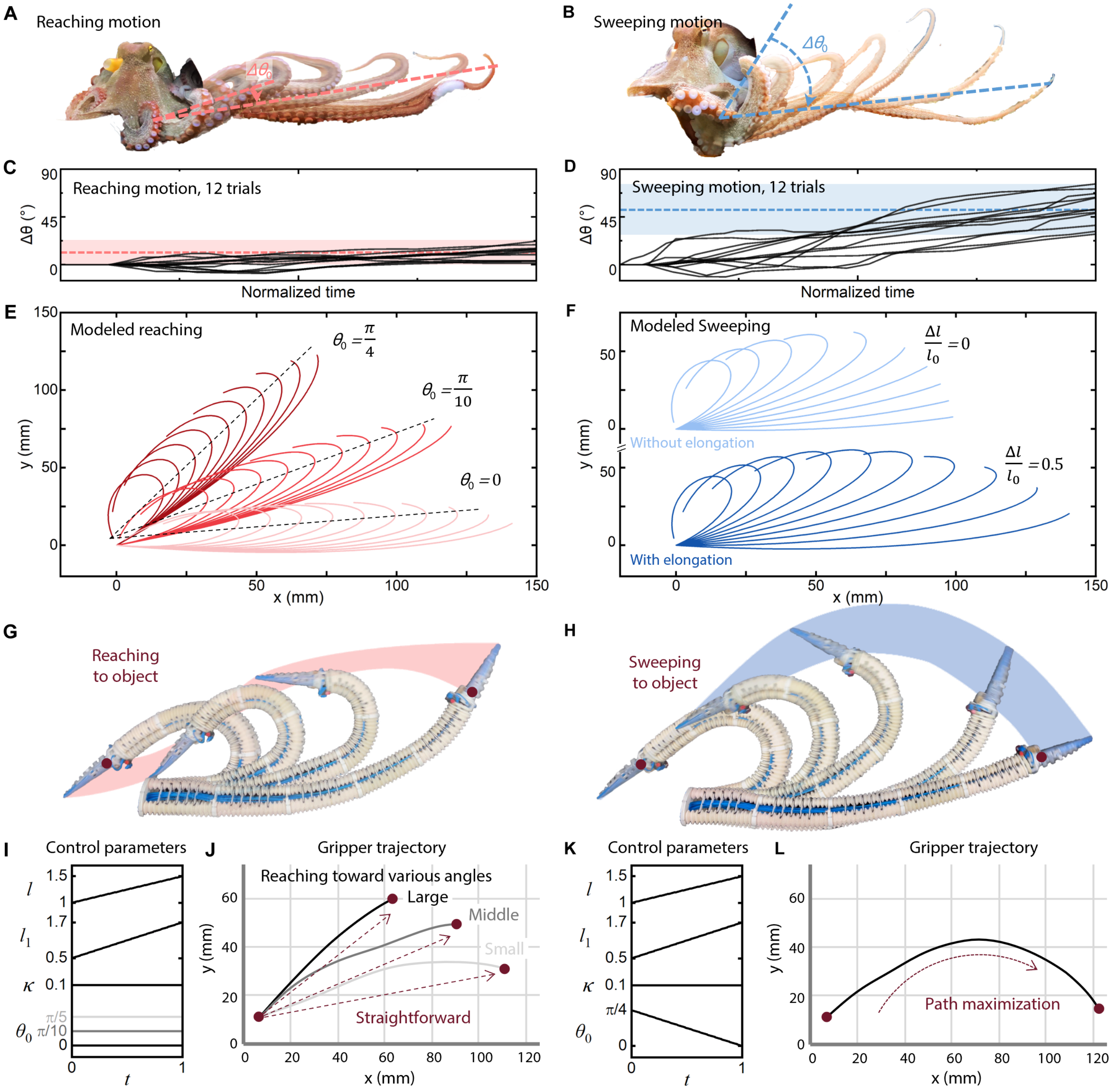

Fig. 3. The E-SOAM's movements based on a bioinspired bend propagation model. The bend propagation of an octopus arm can be classified in two ways based on the deflection angle ($\Delta\theta_0$) of the bending point during propagation. (**A**) A biological octopus arm reaching with a small deflection angle. (**B**) An octopus arm performing a sweeping motion with a large angle deflection. (**C**) Deflection angles from 12 observations of an octopus performing a reaching motion (average $\Delta\theta_0$ is 12°). (**D**) Deflection angles from 12 observations of an octopus performing a sweeping motion (average $\Delta\theta_0$ is 53°). MATLAB plots of the reaching motion (**E**) in different directions ($\theta_0 = 0$, $\pi/10$, and $\pi/4$; $\Delta\theta_0 = 0$; $\Delta l/l_0 = 0.5$) and the sweeping motion (**F**) with and without elongation ($\Delta\theta_0 = -\pi/4$; $\Delta l/l_0 = 0, 0.5$), both modeled according to the classical rose line equation in polar coordinates. Both a reaching motion with various deflection angles (large, middle, and small) (**G**) and a sweeping motion (**H**) were achieved on the basis of the bend propagation model. (**I**) Reaching motion control parameters ($\Delta\theta_0 = 0$; $\Delta l/l_0 = 0.5$). (**K**) Sweeping motion control parameters ($\Delta\theta_0 = -\pi/4$; $\Delta l/l_0 = 0.5$). (G and H) The trajectories of the terminal gripper (highlighted areas) during the reaching and sweeping motions. The reaching trajectories in (**J**) follow a relatively straightforward point-to-point line, whereas (**L**) shows a parabolic path.

where $f(t)$ represents the posture curve of the octopus's arm at time t and the variables $[k_1, \ k_2, \theta_m]$ reflect the shape of the curve, which can derive from the parameters $\{l(t), l_1(t), \kappa(t), \theta_0(t)\}$.

Both reaching and sweeping motions can be described with Eq. 1 by providing the parameters $\{l(t), l_1(t), \kappa(t), \theta_0(t)\}$. The reaching motion can be described by changing $\theta_0(t)$. Figure 3E shows reaching toward different angles, with $\theta_0 = 0$, $\pi/10$, and $\pi/4$, while the arm elongated at an average rate of $\Delta l/l_0 = 0.5$. In Fig. 3F, the sweeping motion is shown when $\theta_0(t)$ varied from 0 to $\pi/4$, both with ($\Delta l/l_0 = 0.5$) and without ($\Delta l/l_0 = 0$) arm elongation. We provide details about the modeling process and how the four parameters affect the bend propagation of E-SOAM in movie S8 and the "Modeling bend propagation of octopus arm" section.

The reaching model was further discretized (*27*) for the kinematics control of E-SOAM (fig. S11, D to G, and the "Modeling bend propagation of octopus arm" section). Figure 3, G and H shows the reaching and sweeping motions of E-SOAM with the control parameters in Fig. 3, I and K, respectively. The trajectories of the E-SOAM terminal gripper are plotted (in red and blue) in Fig. 3, G and H. The reaching trajectory produced a more straightforward point-to-point line (Fig. 3J), whereas the sweeping motion produced a parabola-shaped path (Fig. 3L).

The E-SOAM's autonomous grasping ability, via both reaching and sweeping, was demonstrated by synergistically combining the proprioceptive terminal gripper and the soft arm (fig. S13 and movies S9 and S10). The E-SOAM can accomplish a reaching, grasping, and withdrawing task at a distance (Fig. 4A). To illustrate this, the E-SOAM began by inflating itself to unfold its arm rapidly. The pneumatic flow rate results during the reaching process show that the actuation of the E-SOAM was propagated from segment 1 to segment 5, with only one segment activated at a time (Fig. 4B). When the suckers touched the target object, sensory feedback triggered the terminal gripper to actuate. The gripper fully grasped the target when the reconstructed bending curvature reached a stable value. Then, the E-SOAM withdrew the target by shortening the arm (Fig. 4A). The entire reaching-grasping-withdrawing process was completed within 20 s. We considered the reaching motion a simple but efficient strategy for capturing a target, because it can reduce the control complexity by propagating the arm's actuation segment by segment.

During the sweeping motion (Fig. 4C), the five segments were activated one after another and continuously activated for the rest of the process, resulting in an inverted pyramid shape of actuation flow versus time (Fig. 4D). This differed from the actuation flow control for reaching, which actuated only one segment at a time (Fig. 4B). Such complex actuation increased the operational workspace and search area of the arm. As Fig. 4, E and F shows, by applying the same propagating pneumatic actuation strategy and actuating different numbers of segments (from one to five at a time), the arm can still perform both reaching and sweeping motions (movie S11). The trajectories of the terminal gripper expanded outward and increased as the number of actuated segments increased (Fig. 4, E and F). The operational workspace achieved by sweeping (Fig. 4F) was more extensive than reaching (Fig. 4E), showing possible benefits for mixed actuation modes for searching and grasping objects in different domains.

Human haptic interface

Figure 5A shows the liquid metal circuit–based soft wearable finger glove fabricated to interactively control the E-SOAM (Fig. 5A, fig. S14, and the "Fabricating the soft wearable haptic glove" section). This finger glove has two primary functions: to capture the posture and bending motion of a human finger to control the movement of the E-SOAM and to transfer haptic feedback from the suction gripper to a finger. To perform the first function, the finger's acceleration and attitude (x-axis acceleration a_x, pitch angle α, and roll angle β) were calculated by an inertial measurement unit (IMU) sensor to control E-SOAM's motion toward the target (Fig. 5A and movie S12). The strain sensors on the top of the glove captured the bending of the finger to similarly bend the terminal gripper (fig. S14, D and E; movie S13; and the "Controlling E-SOAM with the wearable glove" section). To perform the second function, the wearable finger glove was fabricated with three suction cups inside the ventral surface of the finger glove. When the E-SOAM suckers were attached to an object, a vacuum was applied to the inner suction cups to pull the skin on the finger (Fig. 5, B and C), thus converting the robot's sensation into actual human sensation (fig. S14C). The operator could even distinguish the softness of the attached objects (from 55 kPa to 3000 mPa) through the terminal gripper and wearable finger glove's haptic feedback (fig. S15, movie S14, and Supplementary Methods).

We showed that a human can move one finger to remotely and interactively control the in-plane reaching and grasping of the E-SOAM (fig. S16A and movie S15). Also, a human operator could use the E-SOAM to search for and grasp a target using haptic feedback alone (for example, with eyes covered; movie S16). Figure 5D shows that when the operator swept his finger at a low speed ($a_x = -0.1$ m/s^2, $\Delta\alpha > 1$), the E-SOAM performed a sweeping motion without elongation and failed to grip the object. The bending and suction sensory feedback signals showed that the terminal gripper did not attach to any object. Figure 5E shows that when the operator swept his finger at a high speed ($a_x = -0.2$ m/s^2, $\Delta\alpha > 1$), the E-SOAM performed a sweeping motion with elongation. When the E-SOAM's suckers were attached to the object, the operator sensed the suction and bent his finger to grasp the object (Fig. 5F). Last, the operator pulled back his finger ($a_x = 0.1$ m/s^2, $\Delta\alpha < 1$) and withdrew the arm of the E-SOAM (Fig. 5G). Figure 5H shows the bending and suction sensory data throughout the grasping process. The parameters used to control the E-SOAM are given in the "Reaching and sweeping trials" section.

DISCUSSION

In contrast to previously developed continuous manipulators that rely on external visual feedback (*28*–*31*) and soft sensors that transmit signals via a tether (*32*, *33*) (table S2), E-SOAM integrates a highly stretchable, on-body electronic circuit that includes multiple sensing units (bending, suction, and temperature), an IC processing module, and a wireless communication module. E-SOAM has a scalable six-segment body that outperforms those of other scalable robots (*28*–*32*, *34*) whose control difficulties increase with the number of segments. Because E-SOAM uses the bend propagation kinematic control strategy of an octopus, it provides a large workspace while retaining constant and low control complexity (*33*, *35*). Compared with previously described soft continuous manipulators, E-SOAM has a bidirectional human-assisted control interface. Specifically, the wearable finger glove produces suction sensations on a human finger. Because of the gripper's embedded sensory response system and the arm's low control complexity, an operator can interactively use E-SOAM to perform in-plane and out-of-plane grasping with a single finger. With the development of E-SOAM, we establish a unified mode of interaction between a soft robot, human, and the environment and broaden how stretchable electronics-integrated bioinspired autonomous systems can manipulate interactively in a large domain.

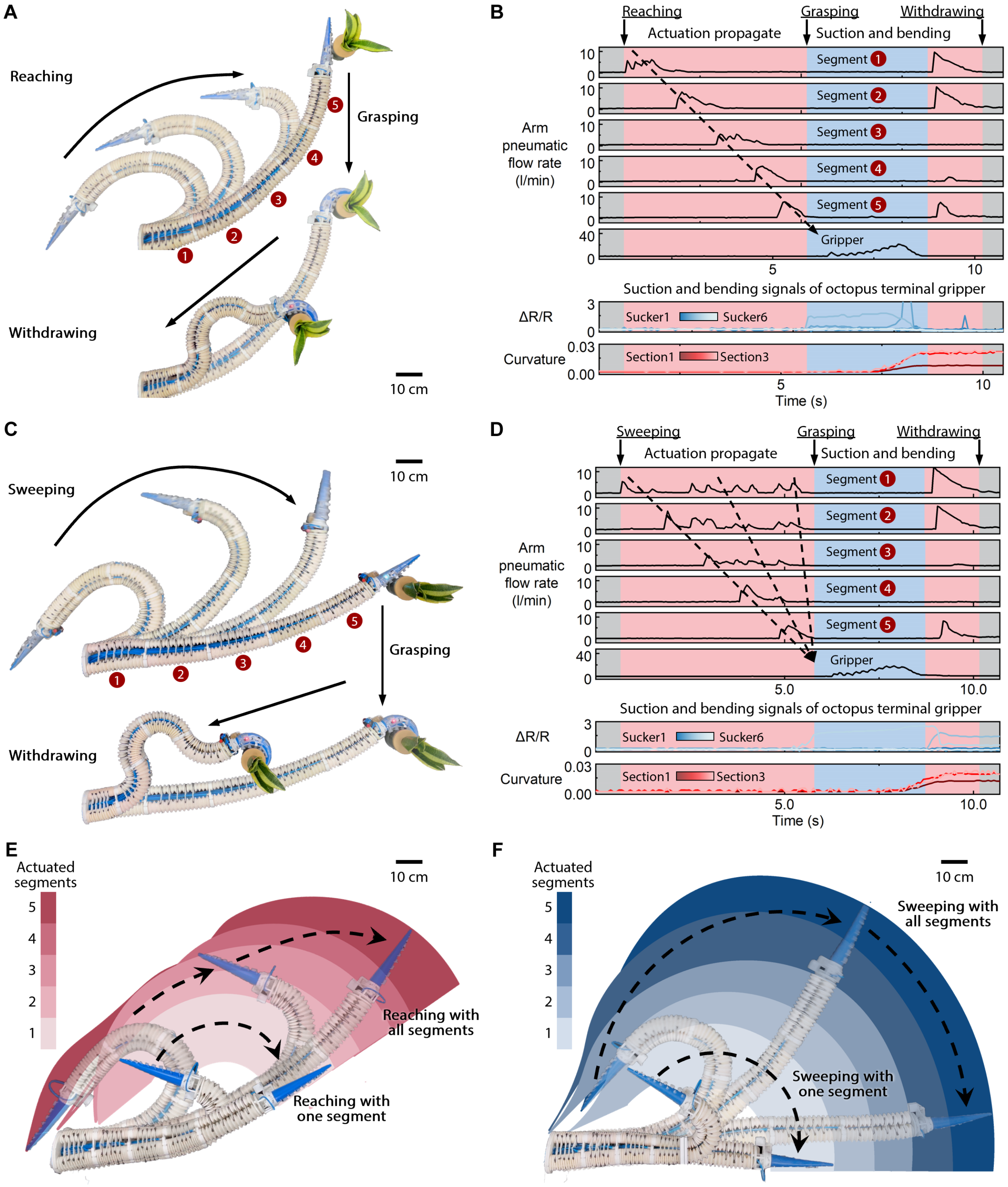

Fig. 4. Comparison of reaching and sweeping motions of E-SOAM. (**A**) E-SOAM's entire bioinspired reaching-grasping-withdrawing process ($\theta_0 = \pi/5$; $\Delta\theta_0 = 0$; $\Delta l/l_0 = 0.8$) and (**B**) the flow rate of E-SOAM's pneumatic segments and the terminal gripper's bending and suction sensory data during the process. (**C**) E-SOAM's sweeping-grasping-withdrawing process ($\Delta\theta_0 = -\pi/4$; $\Delta l/l_0 = 0.5$) and (**D**) corresponding flow rate and the terminal gripper's bending and suction sensory data during the process. The workspace of E-SOAM during both reaching (**E**) and sweeping (**F**) is provided when actuating different numbers of segments (from 1 to 5). The highlighted areas show the terminal gripper's trajectories.

In terms of current limitations, the liquid metal sensing/processing network was only integrated into the distal terminal gripper. In contrast, an octopus receives sensory feedback across an entire arm, which undoubtedly enlarges its sensing and manipulating area. We will expand our sensing/processing network to the entirety of E-SOAM's arm/suckers in the future. Additionally, although the

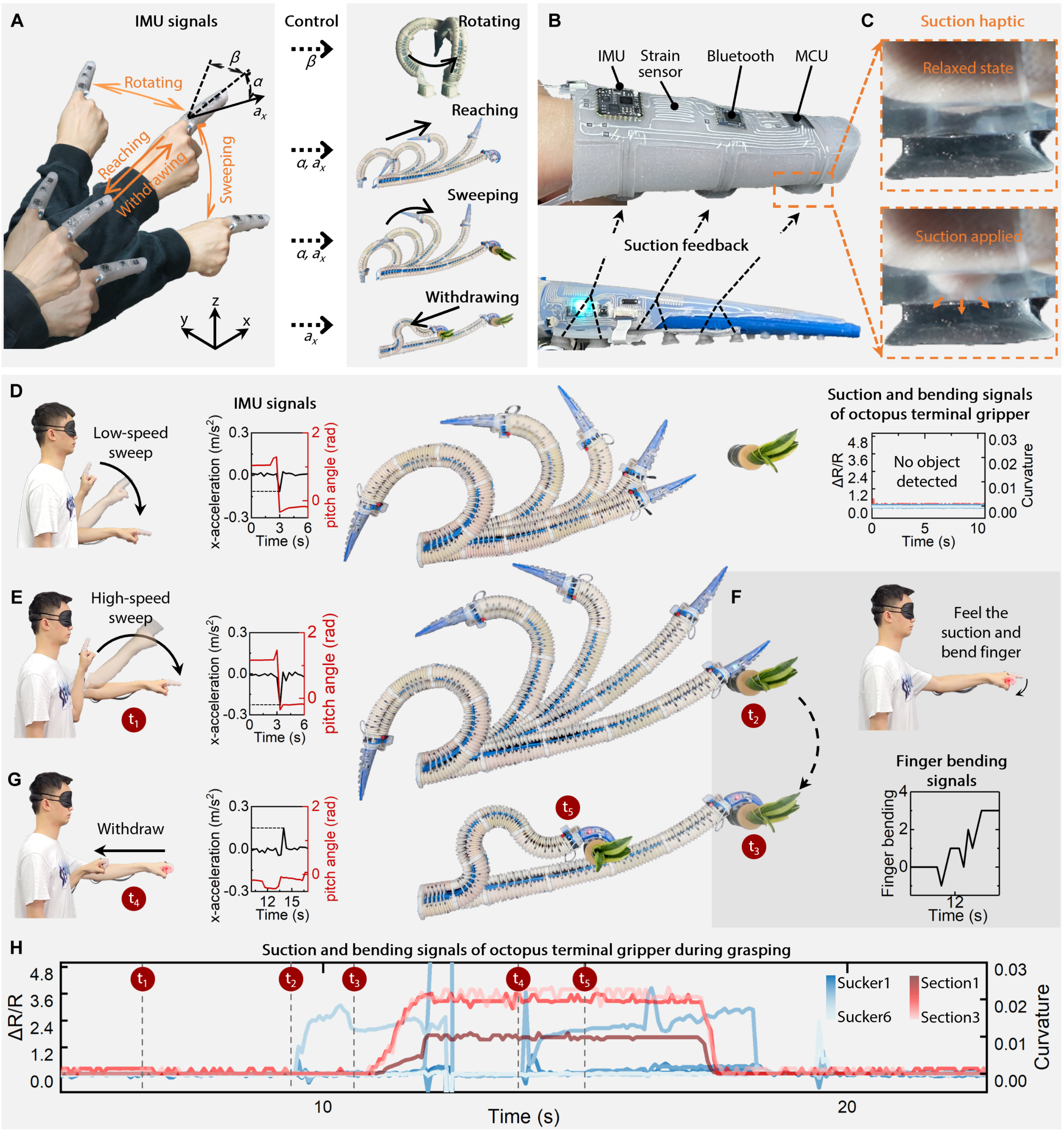

Fig. 5. In-plane bend propagation with haptic feedback guiding E-SOAM control. (**A**) The soft wearable haptic device with liquid metal circuits used to capture the x-acceleration (a_x), pitch angle (α), and roll angle (β) of a human finger for controlling the rotating, reaching, sweeping, and withdrawing motion of the E-SOAM (see movie S12). (**B**) Three inner suction cups on the inner ventral surface of the haptic device transfer sensory feedback from the terminal gripper suctions to a human finger. (**C**) Detailed view of the suction applied on a finger to create haptic interaction between the terminal gripper and a finger. (**D** to **H**) A human operator can sense and control E-SOAM to detect and grasp an object with the haptic device with his eyes covered. (D) When the operator swept a finger at a low speed ($a_x = -0.1$), making E-SOAM sweep without elongation, it failed to grip the object. The sensory feedback showed that no object was detected. (E) When the operator swept a finger at a high speed ($a_x = -0.2$), it caused the E-SOAM to sweep with elongation. (F) The operator felt the finger suction (signifying object detection) and bent the finger, causing E-SOAM to attach to and grasp the object. (G) The operator withdrew the arm by pulling back the finger ($a_x = 0.1$). (H) The E-SOAM's bending and suction sensory signals during the entire sweeping and grasping process.

haptic feedback applied on human finger provides important guidance for the control of E-SOAM, it requires an additional vacuum supply, which partially restricts the movement of a human operator. For a future study, we suggest the adoption of advanced technologies like wearable fluidic pumps (*36*) or vibration systems (*37*) to achieve a fully wireless and untethered human-machine wearable interface. Last, an octopus can perform more complex motions besides bend propagation. E-SOAM's redundant degrees of freedom also make it capable of performing more varied, complex octopus-like movements (fig. S17 and movie S17), which is worth further exploration.

MATERIALS AND METHODS

Fabricating a liquid metal–based stretchable electronic circuit

Figure S1 shows the fabrication steps of the liquid metal–based stretchable electronic circuit: First, we printed a liquid metal circuit pattern on a polyvinyl chloride (PVC) sheet and then poured silicone (Ecoflex 0030, Smooth-On Inc., USA) to cover the printed pattern. After the silicone cure, the circuit was placed and treated in a −140°C environment for 30 min until we removed the PVC sheet and transferred the liquid metal to a silicone substrate. After transferring the liquid metal to the silicone substrate, we placed IC chips and added intermediate material (704 Silicone, Nanda Inc., China) at the edges of the IC chips. Last, we poured another layer of silicone and encapsulated the circuit. After the encapsulation was cured, we cut the circuit into the desired shape using a laser cutter (VLS 2.30DT, Universal Inc., USA).

Intermediate material optimization

The liquid metal used for the E-SOAM is intrinsically stretchable and stable for electrical conduction while undergoing large expansion. However, this expansion can lead to delamination between the IC chip and the soft substrate. To avoid such delamination, which might result in circuit failure, we embedded intermediate material (704 silicone, Young's modulus $E_2 = 660$ kPa) between the soft substrate (Ecoflex 00-30, $E_1 = 69$ kPa) and rigid IC chips to reduce the strain at the interface between the chip and the substrate.

To investigate how the intermediate material affected the stretchability of the circuit, we considered a soft substrate (150 mm by 60 mm by 2 mm) with a rigid silicone chip (10 mm by 10 mm by 1.5 mm) inserted inside. We tested intermediate materials with different shapes, including circular, oval, annular, square, rounded square, rectangular, and rhombic (fig. S2), all of which had the same area (500 mm^2) and thickness (2 mm). The soft substrate was defined to be hyperelastic material with a shear modulus of 0.2 MPa and a modulus of 2000 MPa. The rigid chip was defined to be linear elastic material with an elastic modulus of 110 GPa and a Poisson ratio of 0.1. The intermediate material was defined to be hyperelastic material with a shear modulus of 1 MPa and a bulk modulus of 2000 MPa. To assess the delamination between the soft material and rigid chip, we calculated the strain in the circuit's middle plane coinciding with the top surface of the rigid silicon chip when stretched to 170% of its original length.

Simulation results show that intermediate material in any shape can reduce the strain at the interface between the soft material and rigid chip compared with the unit without intermediate material ($\varepsilon = 0.2669$). The smallest interfacial strains were found with the square-shaped ($\varepsilon = 0.0182$) and rounded square–shaped ($\varepsilon = 0.0189$) cases, which reduced strain by a factor of about 14 compared with the case without intermediate material. Because creating truly square-shaped intermediate material is quite challenging during actual fabrication, we instead used a rounded square shape for the stretchable electronic circuit. By adding intermediate material, the peak strain point moved from near the interface between the soft substrate and the rigid chip to near the interface between the soft substrate and the intermediate material. Nevertheless, the bond between the soft substrate and intermediate material (two silicone rubbers) was stronger than that between silicone rubber and the rigid chip (with peel strength >0.7 N/m) (*38*).

Stretching tests of the stretchable electronic circuit

We tested the stretchability of the electronic circuit with and without intermediate material. The stretchable electronic circuit has a sensing unit (one horizontally placed sensor and one vertically placed sensor), a microcontroller, a wireless communication unit (Bluetooth), and a light-emitting diode (LED) for display (fig. S3A). We clamped the two sides of the circuit via three-dimensional (3D)–printed clamps and then used a robotic arm (MOTOMAN MH3F, YASKAWA Inc., Japan) to pull the circuit upward at a rate of 5 mm/s. The horizontal and vertical resistances were calculated and transmitted by the wireless module on the circuit.

After adding intermediate material, the electronic circuit was stretched up to 360% horizontally (fig. S3D and movie S2) and up to 260% vertically (fig. S3E). The horizontal and vertical resistances during the experiments are shown in fig. S3 (F and G). We also validated the circuit's sensing ability for 15 min and found negligible sensor drift (fig. S3H). The circuit also showed good repeatability after being stretched 300 times (fig. S3I). When stretched in an underwater environment (fig. S3J), the circuit could process and transmit data at a depth of 1 m (fig. S3K).

Because inflating soft actuators often causes membrane stretching, we tested the stretchable electronic circuit with several sensors and silicon components under inflated conditions. A circuit membrane with strain sensors along the radial and circumferential directions, pressure sensor, and LEDs was inflated to expand (fig. S3L). When inflating the circuit, the resistance of the strain sensors increased, and the LEDs lit up as the expansion increased. The expanded circuit could control the inflation by sensing the expansion rate (the surface area increased up to 270% of its original) and external tactile stimuli, such as a finger pressing on the sensor (fig. S3, M and N; also see movie S3 for the entire inflation process).

Fabricating the sensorized terminal gripper

A soft electronic network was designed by arranging sensor/processing circuitry to mimic the structure of an octopus arm and suckers while also enabling multidimensional expansion (fig. S4A). According to the FEA results, we mapped the strain distribution on the inflated robot and placed bending sensors at high strain points to collect elongation and expansion data. We then placed connecting wires and processing circuitry around the bending sensors on the surface of the robot (fig. S4B). The circuit design was then simulated to obtain the appropriate strain distribution when expanding the terminal gripper (fig. S4C). The fabrication of the terminal gripper with an embedded electronic network can be divided as follows:

1) The main circuitry layout was printed in the areas shown in fig. S4B and fabricated following the steps shown in fig. S1.

ICs like the microcontroller, Bluetooth chip, analog switch, crystal oscillator, capacitors, resistors, and ribbon cable connector were placed to complete the entire processing circuit (Fig. 2A). Wire crossings were avoided by locally applying a double-layer circuit (Fig. 2A): First, we placed a drop of silicone rubber (Ecoflex 0030) to cover the underlying liquid metal; then after the silicone drop cured, we used a brush to lay liquid metal on the surface of the cured silicone drop. The main circuit was then attached with silicone adhesive (Sil-Poxy, SmoothOn) on the outer surface of the terminal gripper.

2) To enable the suckers to sense their environment, we inserted a sensing circuit in series into six suckers according to the following steps (fig. S5): First, we printed and fabricated the sensing circuit and assembled the circuit with previous 3D-printed model for casting suckers. After that, we poured silicone (Ecoflex 0030) into the mold, added caps to form the cavity of the suckers, and demolded suckers with a sensing circuit after curing.
3) After the two parts were fabricated, the suckers were attached to the terminal gripper, and the sensing circuit was connected to the primary circuit. The complete terminal gripper with an embedded electronic network is shown in Fig. 2A.

Kinematic reconstruction of the bending terminal gripper

We built a single sensor-based kinematic model to reconstruct the bending profile of the terminal gripper in real time (fig. S7A) (*39*). To simplify the process, we divided the terminal gripper into three sections ($i = 1, 2, 3$) and took the bending profile of each one to be a circular arc (fig. S7B). For the ith section, the EL-i and EP-i sensors were used to measure the inflation and calculate the circular arc's geometries $\{\theta_i, R_i\}$. The detailed modeling process can be found in Supplementary Methods.

Evaluating the sensing ability of the suckers

Each of the six suckers with liquid metal circuits inserted into the terminal gripper can sense independently, as fig. S7 (H to J) shows. To test the ability of the suckers to provide feedback on their own suction state, we attached the suckers to a rectangular box and measured changes in resistance resulting from interactions with the box (fig. S7H). Pulling on the left side of the box pulled suckers 1 to 3 down and pressed suckers 4 to 6 up, triggering a decrease and increase in resistance on those two sucker groups, respectively (fig. S7I). Pulling on the right side of the box had the opposite effect, increasing the resistance on suckers 1 to 3 and decreasing it on suckers 4 to 6 (fig. S7J).

The temperature sensor was attached to the liquid metal circuit (purple marker in Fig. 2A) and embedded inside the largest sucker. We tested its ability to sense the azimuth of a heat source (see Fig. 2F, inset image) by placing the gripper near a lit lightbulb. The sucker with the temperature sensor was placed facing the bulb at a distance of $d = 2$ cm, moved away at an interval of 2 cm until it was 10 cm away, and then placed with its back to the bulb. We recorded the changing signal from the temperature sensor and found that at different distances d, the temperature sensing rate differed notably (Fig. 2F). Orienting the sucker to face toward or back to the bulb also greatly affected its ability to sense temperature (Fig. 2F, blue curve). These results were then used to detect the orientation of a heat source (see Fig. 2G).

Then, we evaluated the robustness of the suction and temperature sensory output under stretching of the circuits. In fig. S8A, we attached the tentacle's suckers to a metal block (heated to 90°C); the corresponding infrared images are shown in fig. S8B. Meanwhile, we inflated the gripper to mimic its operation state, where the circuit was stretched along the expansion direction. Figure S8C shows that the temperature sensors' outputs can respond to temperature change. In contrast, the temperature did not notably affect the suction sensory output.

Soft segments of E-SOAM

E-SOAM comprises a five-segment soft arm and a terminal gripper embedded with an electronic circuit network (fig. S10, A and B). The E-SOAM has a total length of 1.2 m. For each segment of the soft arm, three silicone bellows were connected in parallel. In total, 16 pneumatic actuators were applied to control the E-SOAM. Figure S10C shows the cross-sectional view of the pneumatically actuated silicone below. The segment can elongate or shorten by inflating/deflating the three bellows of the segment. We characterized the length-pneumatic pressure relationship of one soft segment, as shown in fig. S10 (D and E). The soft segment has an original length of 20 cm (0 kPa); a single segment can be elongated to 35 cm (1.75 times its original length) when inflated to 60 kPa. In the current study, we elongated the soft arm up to 30 cm (40 kPa, 1.5 times the original length), which is biologically relevant to our observed average elongation (1.53 times) of the biological octopus arm (*3*).

Modeling bend propagation of octopus arm

To observe the bend propagation of the live octopus (*Octopus vulgaris*), we used a moving rod to attract a live octopus to reach its arm to the rod. Then, we captured videos from the lateral view of the octopus (movies S6 and S7). The octopus used in this study complies with the regulations for the Administration of Affairs Concerning Experimental Animals issued by the Institutional Animal Care and Use Committee of Beijing.

Considering the classical rose line Eq. 1 in polar coordinates that represents the posture curve of an octopus arm at time t, as described in fig. S11A, k_1 determines the distance between the arm base and the bending point; k_2 determines the curvature of the bending point; θ_m represents the rotation angle of the arm tip; and θ_0 represents the rotation angle of the arm base (and is preprogrammed in the kinematic function). Because the rotation angle does not affect the length integral, we ignore the rotation parameter in Eq. 1 as

$$\rho_r(\theta) = k_1 \sin(k_2\theta)(0 < \theta < \theta_m - \theta_0) \tag{2}$$

As shown in fig. S11B, the key parameters $\{l(t), l_1(t), \kappa(t), \theta_0(t)\}$ were used to solve the posture curve Eq. 2 as

$$\begin{aligned} l &= \int_0^{\theta_m-\theta_0} \sqrt{\rho_r^2(\theta)+\rho_r'^2(\theta)}\,d\theta \\ &= \int_0^{\theta_m-\theta_0} \sqrt{k_1^2\sin^2(k_2\theta)+k_1^2k_2^2\cos^2(k_2\theta)}\,d\theta \\ &= k_1 E\left(k_2(\theta_m-\theta_0);\ \sqrt{\frac{k_2^2-1}{k_2^2}}\right) \end{aligned} \tag{3}$$

$$\begin{aligned} l_1 &= \int_0^{\frac{\pi}{2k_2}} \sqrt{\rho_r^2(\theta)+\rho_r'^2(\theta)}d\theta \\ &= \int_0^{\frac{\pi}{2k_2}} \sqrt{k_1^2\sin^2(k_2\theta)+k_1^2k_2^2\cos^2(k_2\theta)}d\theta \\ &= k_1 E\left(\sqrt{\frac{k_2^2-1}{k_2^2}}\right) \end{aligned} \tag{4}$$

$$\kappa = \left|\frac{\rho_r^2(\theta_b)+2\rho_r'^2(\theta_b)-\rho_r(\theta_b)\rho_r''(\theta_b)}{(\rho_r^2(\theta_b)+\rho_r'^2(\theta_b))^{\frac{3}{2}}}\right|\left(\theta_b=\frac{\pi}{2k_2}\right)=\frac{1+k_2^2}{k_1} \tag{5}$$

where $E(\varphi;k)$ represents the incomplete elliptic integral of the second kind and $E(k)$ represents the complete elliptic integral of the second kind. Combining Eqs. 4 and 5, we can solve k_2 from

$$l_1\kappa = (1+k_2^2)E\left(\sqrt{\frac{k_2^2-1}{k_2^2}}\right) \tag{6}$$

Substituting the value of k_2 into Eq. 5, we have

$$k_1 = \frac{1+k_2^2}{\kappa} \tag{7}$$

Substituting the values of k_1 and k_2 into Eq. 3, we have

$$\frac{l}{k_1} = E\left(k_2(\theta_m-\theta_0);\sqrt{\frac{k_2^2-1}{k_2^2}}\right) \tag{8}$$

Using the numerical method for solving the inversion of an incomplete elliptic integral of the second kind (*40*), we can solve for θ_m from Eq. 8 to complete the translation from $\{l, l_1, \kappa, \theta 0\}$ to $\{k_1, k_2, \theta_m\}$. A sequence of time snapshots is shown in fig. S11C to illustrate the curvature change along the length of the model during bend propagation. Because the soft manipulator is composed of segments (fig. S11D), Eq. 1 can be discretely designed as a multilink mechanism that consists of several consistent curvature segments (fig. S11E), shown as

$$f(t,i) = \{\rho(\theta) = k_1\sin(k_2(\theta-\theta_0(t))) \vee \theta_{i-1} < \theta < \theta_i\} \tag{9}$$

where i denotes the ith segment of the soft manipulator.

To obtain the actuation pressure of the soft actuator (fig. S11F), we used a numerical optimization method (*27*) to search for the appropriate arc-length ratio ($s_1 : s_2 : \ldots : s_N = \alpha_1 : \alpha_2 : \ldots : \alpha_N$), and the N segments of the constant curvature arcs optimally fit to Eq. 9. The constant curvature arcs are continuous and can be described by $\{r_i, \theta_i\}$ ($i = 1, 2, \ldots, N$), where r_i denotes the radius of the ith segment of the soft manipulator and θ_i represents the arc angle of the ith segment. The chamber pressure $\{P_{ij}\}$ can then be solved under the constant curvature assumption. The simulation results of the discrete bend propagation model can be found in fig. S11G, which shows the soft manipulator in blue and the terminal gripper in red.

We evaluated the function of the four key parameters $\{l, l_1, \kappa, \theta 0\}$ on the bend propagation of E-SOAM. We found that the reaching motion is alterable and can be realized by the E-SOAM by controlling the four key parameters. In fig. S12, we plot the trajectories of the arm's terminal gripper to show what extension the soft arm can reach out for grasping. The parameter $l(t)$ (the total length of the arm) affects the reaching distance of the arm, as fig. S12A shows, for $\Delta l/l_0$ from 0 to 0.5, the working radius of the soft arm differs notably (fig. S12B). The parameter $\theta_0(t)$ (deflection angle) affects the reaching out direction of the soft arm (fig. S12, C and D). The parameter $\kappa(t)$ (bending curvature) affects the width (d) of the bending arm (fig. S12, E and F). The parameter $l_1(t)$ (distance between the bending point and root of the arm) does not notably affect the motion profile of the soft arm but primarily affects the speed of the reaching motion. In fig. S12H ($\{\Delta l/l_0 = 0.5, \kappa(t) = 0.05, \theta_0 = 0\}$), the nominalized time of the reaching motion decreased from 1.94 to 1 when $\Delta l_1/l_{1\_0}$ changed from 1.0 to 1.5 (fig. S12G).

Fabricating the soft wearable haptic glove

The soft wearable haptic device was fabricated following the steps outlined in fig. S14A. First, the glove's main body was fabricated by preinstalling silicone tubes inside the assembled molds to create vacuum channels for the ventral suction cups inside the glove (Fig. 5C), and then we integrated the preprinted stretchable electronic circuit onto the glove and assembled the soft wearable haptic device.

Controlling E-SOAM with the wearable glove

The soft wearable haptic device was connected to the E-SOAM to send control inputs to the robot and receive sensory signals back from it. As fig. S14B shows, the three inner suckers and the inserted LEDs correspond to the three sucker groups: 1 and 2, 3 and 4, and 5 and 6. When the gripper's suckers attached to an object, a vacuum was applied to the suction cups on the inside of the finger glove, and its LEDs lit up to signal adhesion (fig. S14C). We calibrated the resistance change measured by the strain sensor when a finger bent to different angles (fig. S14D) and mapped it to the terminal gripper's actuation. This allowed the soft wearable haptic device to control the bending of the terminal gripper (fig. S14E and movie S13).

The IMU chip and the Bluetooth chip on the haptic device were used to generate and transfer control instructions to the E-SOAM (Fig. 5A and movie S12). Four different kinds of instructions were generated: For the rotation used in underwater manipulation, we mounted a pneumatic joint at the base of the E-SOAM to change the working plane of the robot. When a human rotated a finger, the roll angle (β) of the IMU chip rotated E-SOAM accordingly; the reaching motion was controlled by using a constant pitch angle (α) and positive x-axis acceleration (a_x) with a finger pointing forward; the sweeping motion was controlled by using a varying pitch angle (α) and positive x-axis acceleration (a_x) with a waving finger; and the withdrawing motion was controlled by negative x-axis acceleration (a_x) with a finger pulling back.

Reaching and sweeping trials

Reaching and sweeping trials for the E-SOAM were conducted on a table to balance the effects of gravity. To reduce friction, we used ball transfers below each segment joint. For the reaching motion shown in Fig. 3G, the parameters used to control the E-SOAM were $\{l(t) = 1 + 0.5t;\ l_1(t) = 0.5 + 1.2t;\ \kappa(t) = 0.1;\ \theta_0(t) = 0, \pi/10, \pi/5;\ t$ indicates normalized time$\}$ (as shown in Fig. 3I, fig. S13A, and movie S9). Once the E-SOAM's suckers touched the target, it bent its terminal gripper, and its sensors measured increased resistance.

The sweeping motion shown in Figs. 3H and 4C was executed with parameters $\{l(t) = 1 + 0.5t;\ l_1(t) = 0.5 + 1.2t;\ \kappa(t) = 0.1;\ \theta_0(t) = \pi(1 - t)/4\}$ (Fig. 3K). The same motion was repeated three times with the target placed at different locations along the E-SOAM's path. The results showed that if the target was along the trajectory, the sensory network on the suckers immediately triggered the gripper to bend and grasp, thus maximizing the grasp area (fig. S13B and movie S10). The reaching-grasping-withdrawing process shown in Fig. 4A was controlled with parameters $\{l(t) = 1 + 0.5t;\ l_1(t) = 0.5 + 2t;\ \kappa(t) = 0.1;\ \theta_0(t) = \pi/5\}$. The glove-controlled reaching motion without elongation shown in Fig. 5D was controlled with parameters $\{l(t) = 1;\ l_1(t) = 0.5 + 0.8t;\ \kappa(t) = 0.08;\ \theta_0(t) = \pi(1 - t)/3\}$, and the reaching motion with elongation in Fig. 5E was controlled with $\{l(t) = 1 + 0.5t;\ l_1(t) = 0.5 + 0.8t;\ \kappa(t) = 0.08;\ \theta_0(t) = \pi(1 - t)/3\}$.

The underwater sweeping motion shown in Fig. 1E was executed with parameters $\{l(t) = 1 + 0.5t;\ l_1(t) = 0.5 + t;\ \kappa(t) = 0.08;\ \theta_0(t) = \pi(1 - 0.3t)/5\}$ when the operator thrust his finger down (t_3, $a_x = -0.7$, $\Delta\alpha > 1$) (Fig. 1C and fig. S16C). The rotation of the sweeping plane was controlled with a rotating joint mounted to the base of E-SOAM. The instruction of the rotation was given when the operator turned his elbow rightward (t_2, $\Delta\alpha < 1$, $\Delta\beta > 1$) (Fig. 1B and fig. S16C), and the instruction of retrieving the object was given when the operator withdrew the finger (t_6, $a_x = 0.25$, $\Delta\alpha < 1$) (Fig. 1E and fig. S16C). Figure S16D shows the bending and suction sensory data of the E-SOAM during the entire grasping process.

Supplementary Materials

This PDF file includes:

Methods
Figs. S1 to S17
Tables S1 and S2

Other Supplementary Material for this manuscript includes the following:

Movies S1 to S17
Data file S1
MDAR Reproducibility Checklist

REFERENCES AND NOTES

1. Y. Gutfreund, T. Flash, G. Fiorito, B. Hochner, Patterns of arm muscle activation involved in octopus reaching movements. *J. Neurosci.* **18**, 5976–5987 (1998).
2. Y. Yekutieli, R. Sagiv-Zohar, B. Hochner, T. Flash, Dynamic model of the octopus arm. II. control of reaching movements. *J. Neurophysiol.* **94**, 1459–1468 (2005).
3. S. Hanassy, A. Botvinnik, T. Flash, B. Hochner, Stereotypical reaching movements of the octopus involve both bend propagation and arm elongation. *Bioinspir. Biomim.* **10**, 035001 (2015).
4. G. Sumbre, Y. Gutfreund, G. Fiorito, T. Flash, B. Hochner, Control of octopus arm extension by a peripheral motor program. *Science* **293**, 1845–1848 (2001).
5. P. P. C. Graziadei, H. T. Gagne, Sensory innervation in the rim of the octopus sucker. *J. Morphol.* **150**, 639–679 (1976).
6. R. Baines, S. K. Patiballa, J. Booth, L. Ramirez, T. Sipple, A. Garcia, F. Fish, R. Kramer-Bottiglio, Multi-environment robotic transitions through adaptive morphogenesis. *Nature* **610**, 283–289 (2022).
7. G. Li, X. Chen, F. Zhou, Y. Liang, Y. Xiao, X. Cao, Z. Zhang, M. Zhang, B. Wu, S. Yin, Y. Xu, H. Fan, Z. Chen, W. Song, W. Yang, B. Pan, J. Hou, W. Zou, S. He, X. Yang, G. Mao, Z. Jia, H. Zhou, T. Li, S. Qu, Z. Xu, Z. Huang, Y. Luo, T. Xie, J. Gu, S. Zhu, W. Yang, Self-powered soft robot in the Mariana Trench. *Nature* **591**, 66–71 (2021).
8. N. T. Jafferis, E. F. Helbling, M. Karpelson, R. J. Wood, Untethered flight of an insect-sized flapping-wing microscale aerial vehicle. *Nature* **570**, 491–495 (2019).
9. Z. Zhakypov, K. Mori, K. Hosoda, J. Paik, Designing minimal and scalable insect-inspired multi-locomotion millirobots. *Nature* **571**, 381–386 (2019).
10. M. Calisti, M. Giorelli, G. Levy, B. Mazzolai, B. Hochner, C. Laschi, P. Dario, An octopus-bioinspired solution to movement and manipulation for soft robots. *Bioinspir. Biomim.* **6**, 036002 (2011).
11. I. D. Walker, D. M. Dawson, T. Flash, F. W. Grasso, R. T. Hanlon, B. Hochner, W. M. Kier, C. C. Pagano, C. D. Rahn, Q. M. Zhang, Continuum robot arms inspired by cephalopods, in *Unmanned Ground Vehicle Technology VII* (SPIE, 2005), pp. 303–314.
12. W. McMahan, V. Chitrakaran, M. Csencsits, D. Dawson, I. D. Walker, B. A. Jones, M. Pritts, D. Dienno, M. Grissom, C. D. Rahn, Field trials and testing of the OctArm continuum manipulator, in *2006 IEEE International Conference on Robotics and Automation* (IEEE, 2006), pp. 2336–2341.
13. C. Laschi, M. Cianchetti, B. Mazzolai, L. Margheri, M. Follador, P. Dario, Soft robot arm inspired by the octopus. *Adv. Robot.* **26**, 709–727 (2012).
14. Y. Yekutieli, R. Sagiv-Zohar, R. Aharonov, Y. Engel, B. Hochner, T. Flash, Dynamic model of the octopus arm. I. Biomechanics of the octopus reaching movement. *J. Neurophysiol.* **94**, 1443–1458 (2005).
15. R. Kang, A. Kazakidi, E. Guglielmino, D. T. Branson, D. P. Tsakiris, J. A. Ekaterinaris, D. G. Caldwell, Dynamic model of a hyper-redundant, octopus-like manipulator for underwater applications, in *2011 IEEE/RSJ International Conference on Intelligent Robots and Systems* (IEEE, 2011), pp. 4054–4059.
16. T. Wang, U. Halder, H.-S. Chang, M. Gazzola, P. G. Mehta, Optimal control of a soft cyberoctopus arm, in *2021 American Control Conference* (IEEE, 2021), pp. 4757–4764.
17. J. A. Rogers, T. Someya, Y. Huang, Materials and mechanics for stretchable electronics. *Science* **327**, 1603–1607 (2010).
18. S. Xu, Y. Zhang, L. Jia, K. E. Mathewson, K.-I. Jang, J. Kim, H. Fu, X. Huang, P. Chava, R. Wang, Soft microfluidic assemblies of sensors, circuits, and radios for the skin. *Science* **344**, 70–74 (2014).
19. C. Larson, B. Peele, S. Li, S. Robinson, M. Totaro, L. Beccai, B. Mazzolai, R. Shepherd, Highly stretchable electroluminescent skin for optical signaling and tactile sensing. *Science* **351**, 1071–1074 (2016).
20. W. Lee, H. Kim, I. Kang, H. Park, J. Jung, H. Lee, H. Park, J. S. Park, J. M. Yuk, S. Ryu, J.-W. Jeong, J. Kang, Universal assembly of liquid metal particles in polymers enables elastic printed circuit board. *Science* **378**, 637–641 (2022).
21. P. Rothemund, A. Ainla, L. Belding, D. J. Preston, S. Kurihara, Z. Suo, G. M. Whitesides, A soft, bistable valve for autonomous control of soft actuators. *Sci. Robot.* **3**, eaar7986 (2018).
22. D. Drotman, S. Jadhav, D. Sharp, C. Chan, M. T. Tolley, Electronics-free pneumatic circuits for controlling soft-legged robots. *Sci. Robot.* **6**, eaay2627 (2021).
23. F. W. Grasso, "The octopus with two brains: how are distributed and central representations integrated in the octopus central nervous system" in *Cephalopod Cognition*, A.-S. Darmaillacq, L. Dickel, and J. Mather, Eds. (Cambridge University Press, 2014), pp. 94–122.
24. Y. Gutfreund, T. Flash, Y. Yarom, G. Fiorito, I. Segev, B. Hochner, Organization of octopus arm movements: A model system for studying the control of flexible arms. *J. Neurosci.* **16**, 7297–7307 (1996).
25. N. Naserifar, P. R. LeDuc, G. K. Fedder, Material gradients in stretchable substrates toward integrated electronic functionality. *Adv. Mater.* **28**, 3584–3591 (2016).
26. Z. Xie, A. G. Domel, N. An, C. Green, Z. Gong, T. Wang, E. M. Knubben, J. C. Weaver, K. Bertoldi, L. Wen, Octopus arm-inspired tapered soft actuators with suckers for improved grasping. *Soft Robot.* **7**, 639–648 (2020).
27. J. Yu, L. Wang, M. Tan, Geometric optimization of relative link lengths for biomimetic robotic fish. *IEEE Trans. Robot.* **23**, 382–386 (2007).
28. T. Mahl, A. Hildebrandt, O. Sawodny, A variable curvature continuum kinematics for kinematic control of the bionic handling assistant. *IEEE Trans. Robot.* **30**, 935–949 (2014).
29. A. D. Marchese, D. Rus, Design, kinematics, and control of a soft spatial fluidic elastomer manipulator. *Int. J. Robot. Res.* **35**, 840–869 (2016).
30. H. Jiang, Z. Wang, Y. Jin, X. Chen, P. Li, Y. Gan, S. Lin, X. Chen, Hierarchical control of soft manipulators towards unstructured interactions. *Int. J. Robot. Res.* **40**, 411–434 (2021).
31. C. D. Santina, R. K. Katzschmann, A. Bicchi, D. Rus, Model-based dynamic feedback control of a planar soft robot: Trajectory tracking and interaction with the environment. *Int. J. Robot. Res.* **39**, 490–513 (2020).
32. R. L. Truby, C. Della Santina, D. Rus, Distributed proprioception of 3D configuration in soft, sensorized robots via deep learning. *IEEE Robot. Autom. Lett.* **5**, 3299–3306 (2020).
33. M. Giorelli, F. Renda, M. Calisti, A. Arienti, G. Ferri, C. Laschi, Neural network and Jacobian method for solving the inverse statics of a cable-driven soft arm with nonconstant curvature. *IEEE Trans. Robot.* **31**, 823–834 (2015).

34. A. Kapadia, I. D. Walker, Task-space control of extensible continuum manipulators, in *2011 IEEE/RSJ International Conference on Intelligent Robots and Systems* (IEEE, 2011), pp. 1087–1092.
35. B. T. Phillips, K. P. Becker, S. Kurumaya, K. C. Galloway, G. Whittredge, D. M. Vogt, C. B. Teeple, M. H. Rosen, V. A. Pieribone, D. F. Gruber, R. J. Wood, A dexterous, glove-based teleoperable low-power soft robotic arm for delicate deep-sea biological exploration. *Sci. Rep.* **8**, 14779 (2018).
36. M. Smith, V. Cacucciolo, H. Shea, Fiber pumps for wearable fluidic systems. *Science* **379**, 1327–1332 (2023).
37. M. Zhu, S. Biswas, S. I. Dinulescu, N. Kastor, E. W. Hawkes, Y. Visell, Soft, wearable robotics and haptics: Technologies, trends, and emerging applications. *Proc. IEEE* **110**, 246–272 (2022).
38. Liyang kangda new material Co.,Ltd. Technical specifications of Nanda 704 silicone (2022); http://en.nanda-silicone.com/list_25/91.html.
39. Z. Xie, F. Yuan, Z. Liu, Z. Sun, E. M. Knubben, L. Wen, A proprioceptive soft tentacle gripper based on crosswise stretchable sensors. *IEEE/ASME Trans. Mechatron.* **25**, 1841–1850 (2020).
40. J. P. Boyd, Numerical, perturbative and Chebyshev inversion of the incomplete elliptic integral of the second kind. *Appl. Math Comput.* **218**, 7005–7013 (2012).

Acknowledgments: We thank J. Liu for help in liquid metal application and S. Du for finger haptic understanding. C.L. is on leave from the BioRobotics Institute of Scuola Superiore Sant'Anna, Pisa, Italy. **Funding:** This work was supported by the National Science Foundation support projects, China (grant nos. 61822303, T2121003, and 92048302 to L.W.), the National Key R&D Program of China (grant no. 2020YFB1313003 to L.W.), NUS start-up grant RoboLife (A-0009125-02-00 to C.L.), and the Ministry of Education of Singapore (REBOT Project – Rethinking underwater robot manipulation, MOE-T2EP50221-0010 to C.L.).

Author contributions: Z.X., C.L., and L.W. conceptualized this work. Z.X., F.Y., L.T., Z.F., S.M., and G.W. developed the flexible electronics. J.L. developed the robotic arm and reaching model. B.C. acquired the biological data. Z.X., F.Y., J.L., L.T., B.C., Z.F., and S.M. performed experiments. Z.X., F.Y., J.L., T.J., Y.W., and Y.M. visualized data. Z.X., F.Y. J.L., and L.W. wrote the manuscript. All the authors discussed the results and commented on the manuscript. L.W. supervised this study. **Competing interests:** The authors declare that they have no competing interests. **Data and materials availability:** All data needed to evaluate the conclusions in the paper are present in the paper or the Supplementary Materials.

Submitted 14 March 2023
Accepted 31 October 2023
Published 29 November 2023
10.1126/scirobotics.adh7852

Science Robotics

Octopus-inspired sensorized soft arm for environmental interaction

Zhexin Xie, Feiyang Yuan, Jiaqi Liu, Lufeng Tian, Bohan Chen, Zhongqiang Fu, Sizhe Mao, Tongtong Jin, Yun Wang, Xia He, Gang Wang, Yanru Mo, Xilun Ding, Yihui Zhang, Cecilia Laschi, and Li Wen

Sci. Robot. **8** (84), eadh7852. DOI: 10.1126/scirobotics.adh7852

Science Robotics (ISSN 2470-9476) is published by the American Association for the Advancement of Science. 1200 New York Avenue NW, Washington, DC 20005. The title *Science Robotics* is a registered trademark of AAAS.